



Preparation of AgInS₂/TiO₂ composites for enhanced photocatalytic degradation of gaseous *o*-dichlorobenzene under visible light



Baojun Liu^a, Xinyong Li^{a,b,*}, Qidong Zhao^a, Jun Ke^a, Moses Tadé^b, Shaomin Liu^b

^a State Key Laboratory of Fine Chemicals, Key Laboratory of Industrial Ecology and Environmental Engineering (MOE), School of Environmental Science and Technology, Dalian University of Technology, Dalian 116024, China

^b Department of Chemical Engineering, Curtin University, GPO Box U1987, Perth, WA 6845, Australia

ARTICLE INFO

Article history:

Received 14 October 2015

Received in revised form

30 November 2015

Accepted 1 December 2015

Available online 3 December 2015

Keywords:

AgInS₂/TiO₂ heterojunction

Photocatalytic degradation

1, 2-Dichlorobenzene

In situ Fourier transform infrared spectroscopy

ABSTRACT

In this work, the TiO₂ and AgInS₂ heterostructures with different mole ratios were prepared through a simple hydrothermal method. The as-synthesized composites were characterized by field emission scanning electron microscopy (FE-SEM), transmission electron microscopy (TEM), X-ray diffraction (XRD), and X-ray photoelectron spectroscopy (XPS). The results showed that the obtained materials exhibited multi-heterostructures, possessing the orthorhombic phase of AgInS₂, and anatase and rutile phase of TiO₂. Furthermore, the optical properties displayed that a series of AgInS₂/TiO₂ composites could expand the visible-light response range and enhance the absorption intensity by UV–vis diffuse reflection spectroscopy (DRS). The photo-generated carriers were subsequently investigated by the surface photovoltage (SPV) spectra and photoluminescence (PL) technique, and the results demonstrated that the forming heterojunctions greatly depressed the recombination of photogenerated charges in the composites. Finally, the materials were tested as photocatalysts for degradation of gaseous 1, 2-dichlorobenzene (*o*-DCB) under visible-light irradiation, and the degradation process and final products (CO₂) were identified by using *in situ* Fourier transform infrared (FTIR) spectroscopy. The mechanism of enhanced photocatalytic activity was proposed in terms of the quantum calculation of AgInS₂ and the proper band alignment of AgInS₂/TiO₂ composites.

© 2015 Elsevier B.V. All rights reserved.

1. Introduction

Photocatalytic reaction, as an advanced oxidation technology (AOT), has great potential in applications such as the pollutant control and solar energy conversion. TiO₂ is one of the most investigated and promising photocatalysts due to its favorable properties of long-term stability, high photostability and low toxicity [1–4]. However, its wide band gap and relatively high electron-hole recombination rate often result in low quantum yield and poor efficiency of photocatalytic reactions [5]. To address these problems, many approaches, such as the decoration with noble metals [6–8], low-level doping with nonmetal elements [9–11] and the formation of composites with other semiconductor materials [12–14], have been widely and intensively attempted in recent years. Among these methods, the fabrication of heterogeneous composites is one

of the most effective ways to enhance the separation of photo-induced carriers, which could also achieve narrow band gap and take full advantage of solar light, in comparison with the individual components.

Currently, semiconductor materials of ternary chalcogenide I–III–VI (I = Cu, Ag; III = Al, In, Ga; VI = S, Se, Te) have gained much attention because they could exhibit excellent catalytic performances and optical properties, especially, they possess a wider response range in the region of visible light [15–17]. AgInS₂, with direct band gaps of 1.8–2.2 eV, is believed to be one of the most important ternary chalcogenides for its potential applications in fluorescence, solar cells and photocatalytic fields [18–22]. Especially, in the unit cell of the orthorhombic AgInS₂, there exists wurtzite-like structure constructed by InS₄ and AgS₄ tetrahedra, and the unequal bonds of Ag–S and In–S would lead to distortion of the tetrahedra, giving rise to the internal electric field [21]. In a previous study [23], the electric field would be significantly beneficial for the charge separation under illumination, which could enhance the photocatalytic activity. In spite of these advantages of AgInS₂, it is obvious that higher charge recombination rate, lower quantum efficiency, and stronger light etching would

* Corresponding author at: State Key Laboratory of Fine Chemicals, Key Laboratory of Industrial Ecology and Environmental Engineering (MOE), School of Environmental Science and Technology, Dalian University of Technology, Dalian 116024, China. Fax: +86 411 8470 7733.

E-mail addresses: xyli@dlut.edu.cn, xinyongli@hotmail.com (X. Li).

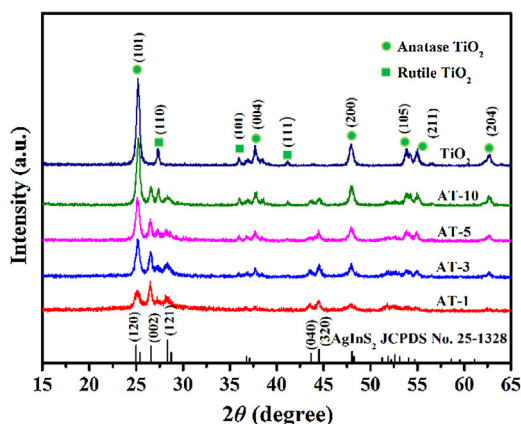


Fig. 1. XRD patterns of TiO_2 and $\text{AgInS}_2/\text{TiO}_2$ composites (AT-1, AT-3, AT-5 and AT-10).

prevent it from large-scale photocatalytic applications for individual components. Thus, the forming heterogeneous structures with other semiconductors should be imperative for electron-hole effective separation and transfer, and would enhance photocatalytic efficiency. Recently, Li et al. [5] reported that the $\text{AgInS}_2/\text{TiO}_2$ composite photocatalysts prepared by a simple one-pot hydrothermal method showed enhanced activity for H_2 production under visible light. Liu et al. [24] reported that the 2D ZnIn_2S_4 nanosheet/1D TiO_2 nanorod heterostructure arrays by a facile hydrothermal process achieved significant enhancement on photoelectrochemical water splitting. Li et al. [25] reported that $\text{CuInS}_2/\text{TiO}_2$ nanotube arrays heterostructure prepared by an ultrasonication-assisted electrodeposition method exhibited enhanced photoactivity for the degradation of 2-chlorophenol (2-CP) under visible light irradiation ($\lambda > 420 \text{ nm}$). From these studies, it could be seen that the hetero-junctions formed by coupling ternary chalcogenide with TiO_2 would significantly enhance photocatalytic reaction activity.

Based on the above considerations, this study was focusing on designing effective and stable hetero-junction structures with narrow band-gap semiconductors for photocatalytic applications. Herein, a series of $\text{AgInS}_2/\text{TiO}_2$ composites has been fabricated by a one-pot hydrothermal method towards photocatalytic degradation of gaseous 1, 2-dichlorobenzene (*o*-DCB) under visible-light irradiation. *o*-DCB, as a model compound of polychlorinated dibenzo-*p*-dioxins and dibenzofurans (PCDDs/PCDFs), has raised wide attention because of their bioaccumulation, high toxicity and carcinogenicity in the environment [26,27]. We demonstrate that mild modification of TiO_2 with ternary chalcogenide AgInS_2 is a promising strategy for enhancing catalytic activity in the elimination of chlorinated volatile organic compounds (Cl-VOCs). Furthermore, the mechanism of photocatalytic performance enhancement over $\text{AgInS}_2/\text{TiO}_2$ composite has been discussed in detail with spectral characterization and quantum chemical calculation methods.

2. Experimental

2.1. Fabrication of $\text{AgInS}_2/\text{TiO}_2$ heterostructure materials

All reagents were analytically pure and used as received without further purification. The $\text{AgInS}_2/\text{TiO}_2$ heterostructure photocatalysts were prepared by a one-step hydrothermal method with some modifications [5]. In a typical synthesis, 0.2 mmol of $\text{In}(\text{NO}_3)_3 \cdot x\text{H}_2\text{O}$, 0.2 mmol of AgNO_3 (the molar ratio of In and Ag is set to 1:1) and 4 mmol of thioacetamide (TAA) were mixed with 60 mL of ultrapure water under vigorous stirring. After half an hour, the TiO_2 (Degussa, P25) was added into the above solution under ultra-sonication, and

then the ratios with In or Ag constituents and TiO_2 were controlled at 1/1, 1/3, 1/5 and 1/10, respectively (so the amounts of TiO_2 are 0.2, 0.6, 1 and 2 mmol, respectively). Then the pH values of the mixed solution were adjusted to about 10, followed by transferring into 100 mL Teflon-lined autoclaves, which were sealed and kept at 180°C for 24 h and then cooled down naturally. Subsequently, the precipitate was filtered and washed with ultrapure water and absolute ethanol several times and dried overnight at 70°C . The composites with molar ratios 1/1, 1/3, 1/5 and 1/10 are denoted as AT-1, AT-3, AT-5 and AT-10, respectively. Similarly, pristine AgInS_2 was also fabricated by the same process above without adding TiO_2 .

2.2. Characterization of catalysts

The crystal structure was determined using X-ray diffractometer (XRD, Rigaku Corporation D/max-2400) with $\text{Cu K}\alpha$ radiation, and the data were obtained in the 2θ range from 15° to 65° . The surface compositions and valence states were conducted by X-ray photoelectron spectroscopy (XPS, Thermo ESCALAB 250XI). The morphology of the synthesized samples was analyzed by using field emission scanning electron microscopy (FESEM, Hitachi SU8010) and transmission electron microscopy (TEM, FEI Tecnai G20). The UV–Vis diffuse reflection spectra (DRS) were recorded by a UV–vis absorption spectrophotometer (JASCO, UV-550) in the region of 200–800 nm. The properties of the defect-related electronic structures were investigated by using photoluminescence (PL) spectra in a fluorescence spectrophotometer (Hitachi F-4500) with the excitation wavelength of 325 nm at room temperature. Surface photovoltage (SPV) spectra were recorded on a home-built measurement system, which consisted of a monochromator (model SBP500, Zolix) and a lock-in amplifier (model SR830-DSP) with an optical chopper (model SR540).

2.3. Photocatalytic degradation evaluations

To evaluate excellent performance of the fabricated photocatalysts, we chose gaseous *o*-DCB as an objective pollutant. The reaction process was conducted in a home-built *in situ* quartz cell with about 130 mL volume [28]. A 500 W Xenon lamp equipped with a UV-cut off filter ($\lambda > 400 \text{ nm}$) was chosen as source of visible light. The catalysts (0.03 g) pressed into the circular pieces were fixed to the holder and then the cell was sealed up at room temperature. At that moment, the liquid *o*-DCB (5 μL) was injected into the reaction cell by micro syringe. After about an hour in the dark, the *o*-DCB completely evaporated to steam and could reach adsorption equilibrium, and the concentration of gaseous *o*-DCB was designated as the initial value. After turning on the light, the IR spectra were recorded by FT-IR (Bruker VERTEX 70) with a resolution of 1 cm^{-1} in the region of 4000 and 500 cm^{-1} . The concentrations of gaseous *o*-DCB in the reaction process were analyzed by integrated area of IR spectra in the region of $1419.58\text{--}1481.30 \text{ cm}^{-1}$. The pollution conversions were calculated as follows:

$$\text{The } o\text{-DCB conversion (\%)} = \left(1 - \frac{[o\text{-DCB}]_t}{[o\text{-DCB}]_0}\right) \times 100\% \quad (1)$$

where $[o\text{-DCB}]_0$ is the initial concentration of gaseous *o*-DCB, and $[o\text{-DCB}]_t$ is the concentration of gaseous *o*-DCB after t hours.

2.4. Calculation methods

The quantum chemical calculations were carried out by the planewave pseudopotential density functional theory (DFT) method within the generalized gradient approximation (GGA) by using the Cambridge serial total energy package (CASTEP) [29]. The unit cell of orthorhombic AgInS_2 (16 atoms) and TiO_2 (30

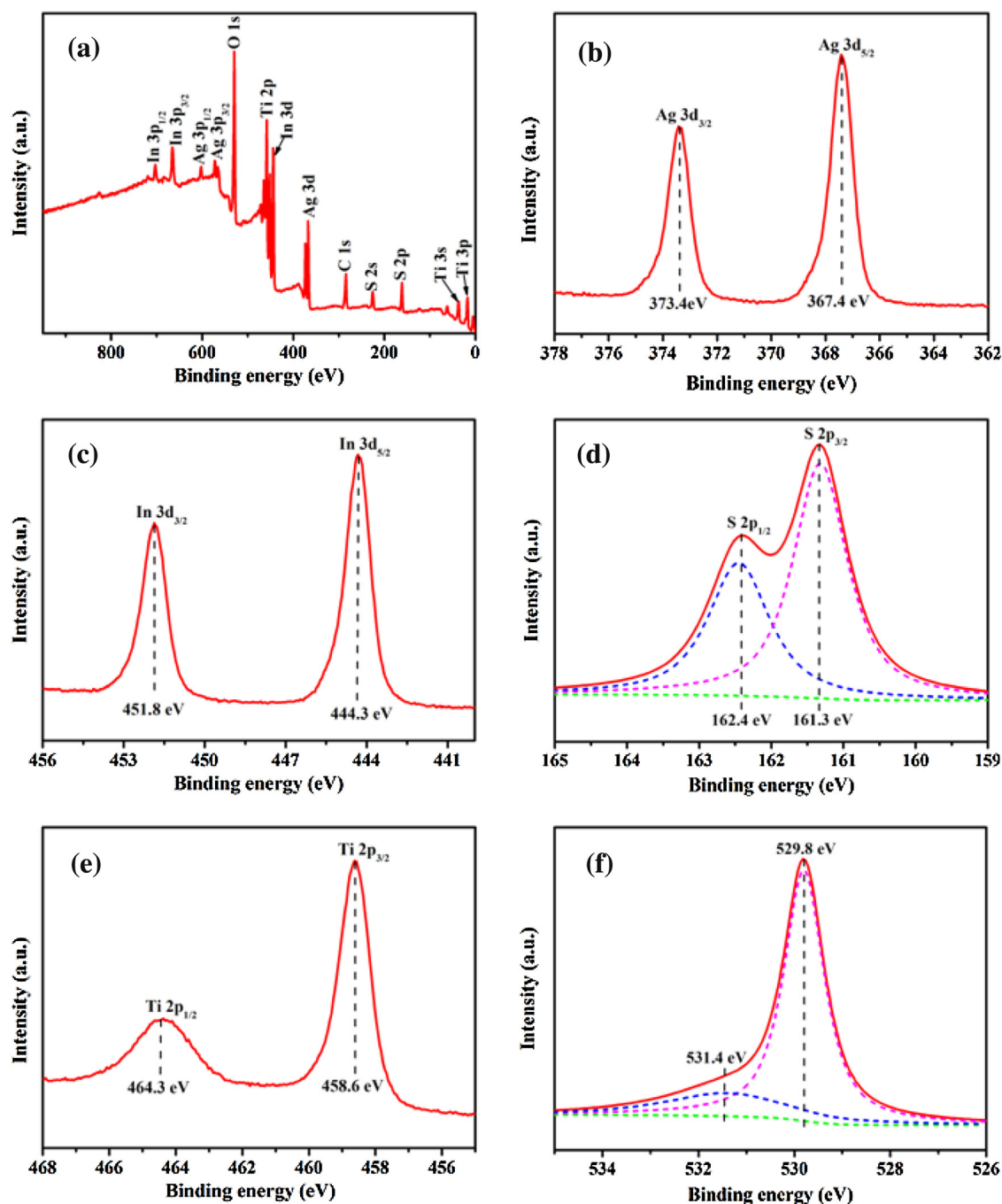


Fig. 2. XPS spectra of AT-5 composite, (a) survey of the sample, (b) Ag 3d spectrum, (c) In 3d spectrum, (d) S 2p spectrum, (e) Ti 2p spectrum and (f) O 1s spectrum.

atoms) was used in the calculations. The crystal lattice parameters of AgInS_2 were adopted from the XRD data. A plane wave basis set was performed with a cutoff energy of 260.0 eV. The valence atomic configurations are $3s^2 3p^4$ for S, $5s^2 5p^1$ for In and $4s^2 4p^6 4d^{10} 5s^1$ for Ag.

3. Results and discussion

3.1. Structure characterization

3.1.1. XRD analysis

Fig. 1 shows the wide-angle XRD patterns for TiO_2 and $\text{AgInS}_2/\text{TiO}_2$ heterostructures with different molar ratios. For the TiO_2 sample, the characteristic peaks, appearing at 2θ : 27.4, 36.1,

37.8, 41.3, 53.9, 55.1 and 62.7, could be ascribed to the diffraction patterns of (1 1 0), (1 0 1), (0 0 4), (1 1 1), (1 0 5), (2 1 1) and (2 0 4) of anatase and rutile phase structure. When coupled with semiconductor AgInS_2 , the composites (AT-x) exhibit multiphase TiO_2 and AgInS_2 peaks with those extra diffraction peaks at 2θ : 26.6, 28.4, 43.7 and 44.5, which are corresponding to the (0 0 2), (1 2 1), (0 4 0) and (3 2 0) plane reflections of the orthorhombic phase AgInS_2 . Furthermore, no other peaks of impurities are observed. As the molar ratios of AgInS_2 and TiO_2 increase, those diffraction peaks of TiO_2 decrease gradually, whereas the peak intensities of AgInS_2 increase. This observation indicates that the particles fabricated are composed of multi-phase heterostructures of AgInS_2 and TiO_2 .

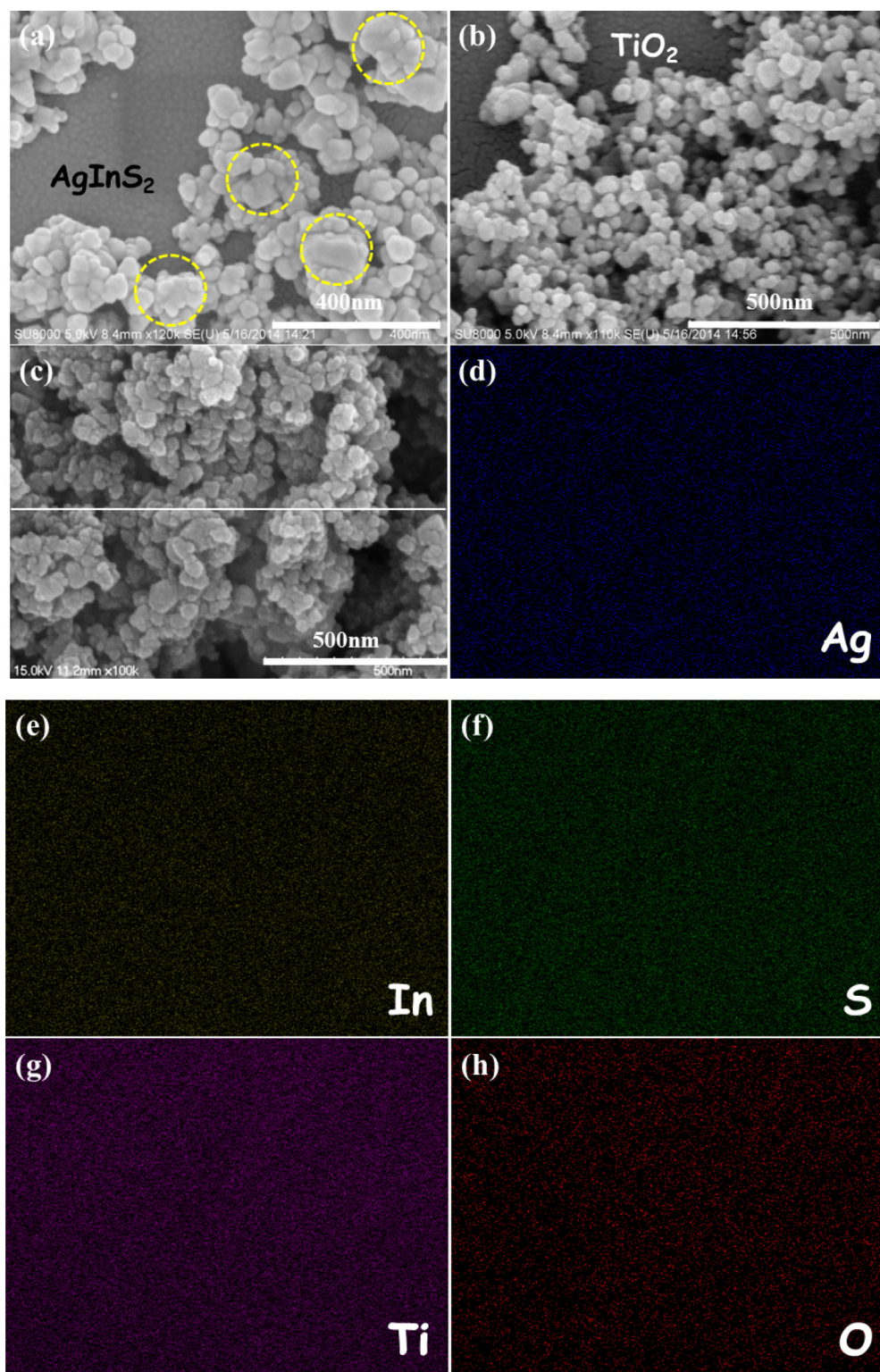


Fig. 3. (a–c) The SEM images of AgInS₂, TiO₂ and AT-5 composites, respectively; and (d–h) the corresponding elemental mapping images for Ag, In, S, Ti and O from the selected area of AT-5.

3.1.2. XPS analysis

To further confirm the surface components and chemical states of AT-5 heterostructures, the materials are detected by XPS and the results are displayed in Fig. 2. From the survey spectrum (Fig. 2a), it is evident that the AT-5 sample is mainly composed of Ag, In, S, Ti and O elements and without other impurities, as well as C element at binding energy 284.6 eV from the referencing spectra or

allogenic substance [28]. Additionally, the ratios of all of the elements in the AT-5 were also investigated by XPS, and it could be seen that an apparent atomic ratio is approximate to stoichiometric proportion (shown in Table S1 in the Supporting information (SI)). High-resolution scan image of the Ag element in Fig. 2b shows two different characteristic peaks at binding energies 373.4 eV and 367.4 eV for Ag 3d_{3/2} and Ag 3d_{5/2}, respectively, which are ascribed

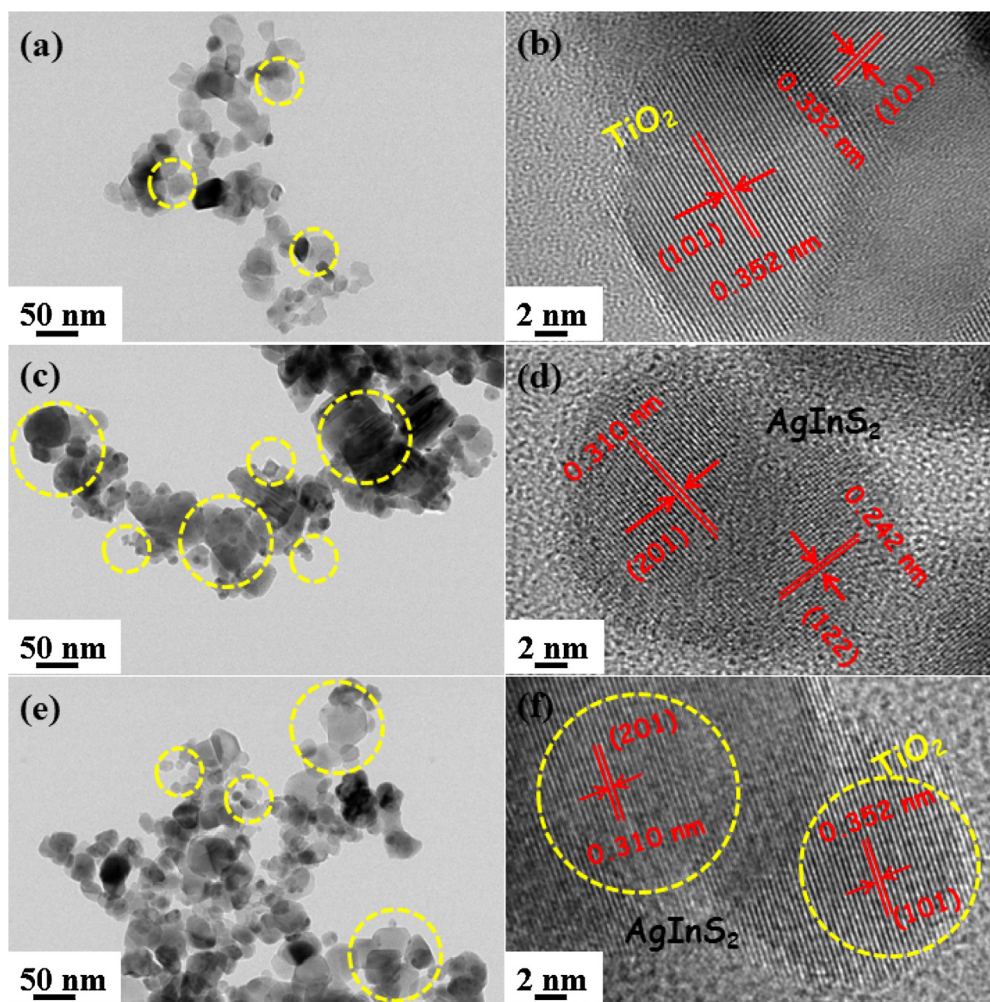


Fig. 4. (a–f) The TEM and HRTEM images of TiO_2 , AgInS_2 and AT-5, respectively.

to the Ag^+ . In addition, the XPS spectra of In 3d and Ti 2p are shown in Fig. 2c and e, respectively, and the peaks at 451.8 and 444.3 eV, as well as 464.3 and 458.6 eV, could be assigned to the characteristic spectra of In^{4+} and Ti^{4+} , respectively. The XPS spectrum of S 2p, with respective binding energies at 162.4 eV for S $2p_{1/2}$ and 161.3 eV for S $2p_{3/2}$, corresponding to the characteristic peaks of S^{2-} , could be deconvoluted into two peaks by Gaussian–Lorentzian fitting method due to its asymmetry in Fig. 2d [22]. Likewise, the peak at 531.4 eV is ascribed to the adsorbed terminal O–H on the surface of catalyst, while the band at 529.8 eV is attributed to the surface lattice oxygen, which is corresponding to the characteristic spectrum of O^{2-} [30].

3.2. Morphologic characterization

3.2.1. SEM

The morphology of pristine AgInS_2 , TiO_2 , and AT-5 nanoparticles was investigated by FE-SEM analysis, as shown in Fig. 3. The bare AgInS_2 is composed of particles with diameters from 20 to 200 nm (Fig. 3a) and shows a broad particle size distribution. On the contrary, TiO_2 particles exhibit regular particles sizes with an average of 25 nm in Fig. 3b. After hydrothermal reaction with AgInS_2 , the AT-5 heterostructure presents significant aggregation, which is similar to the pristine AgInS_2 , but the particle diameters are almost consistent with the TiO_2 nanoparticles, as shown in Fig. 3c. To further investigate elemental composition and distribution uniformity, the elemental maps of the selected area on AT-5 are

displayed in Fig. 3d–h, indicating that homogeneous distribution of Ag, In, S, Ti and O constituting elements in the AT-5 nanoparticles. These analyses demonstrate that AgInS_2 tends to integrate the TiO_2 nanoparticles firmly and then form hetero-junction structures.

3.2.2. TEM and HRTEM

The more detailed morphology of pristine AgInS_2 , TiO_2 , and AT-5 nanoparticles was revealed using TEM and HRTEM. As shown in Fig. 4a, the low-magnification TEM image of TiO_2 is composed of regular particles with an average particle size of 25 nm, and the lattice spacing of around 0.352 nm in the high resolution TEM (HRTEM) image corresponds to the distance of (101) plane of Anatase TiO_2 (Fig. 4b). Additionally, the low-magnification TEM image of bare AgInS_2 exhibits broad distribution in particles sizes and coarse surface, and the lattice spacings of around 0.310 nm and 0.242 nm in the HRTEM image correspond to the distances of (201) and (122) plane of AgInS_2 (Fig. 4c and d), respectively. From Fig. 4e and f, the AT-5 nanoparticles also show the irregular particles and coarse surface, which are similar to the bare AgInS_2 . The HRTEM image of AT-5 reveals that the interplanar spacings of 0.310 nm and 0.352 nm correspond to the (201) and (101) plane of AgInS_2 and TiO_2 , respectively, indicating the formation of $\text{AgInS}_2/\text{TiO}_2$ heterostructure.

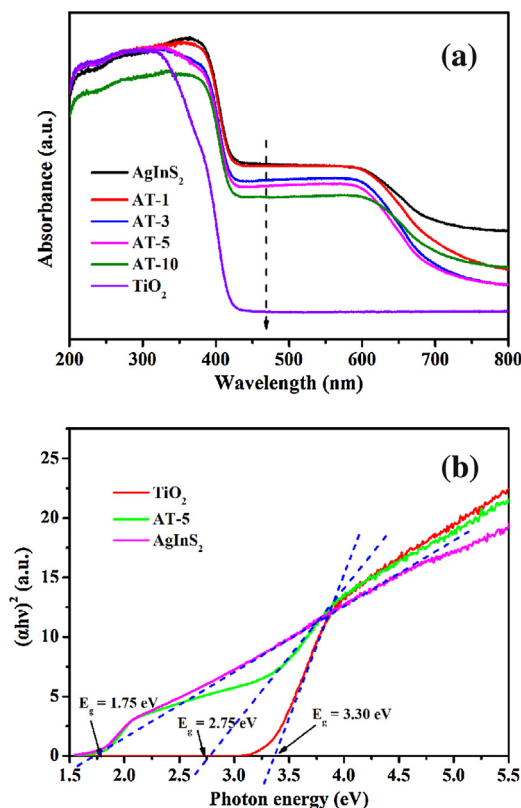


Fig. 5. (a) UV-vis DRS of the samples, and (b) Tauc's plot of TiO₂, AgInS₂ and AT-5 for the band gaps.

3.3. The optical properties

3.3.1. UV-vis DRS spectra

The optical properties of the synthesized nanoparticles are investigated by UV-vis diffuse reflection spectra (DRS). As depicted in Fig. 5a, it could be seen that the pristine TiO₂ mainly exhibits high absorption intensity in the region of UV light, whereas the adsorption edges of the composites significantly extend to the region of visible-light wavelength (400–700 nm). The results suggest that the obtained particles would show enhanced absorption ability under visible light. In addition, the band gap energies of the samples could be evaluated using Tauc's plots: $(\alpha h\nu) = A(h\nu - E_g)^{n/2}$, where α , h , ν , A , and E_g are indicative to the absorption coefficient, Planck's constant, light frequency, constant value, and band-gap energy, and n is 1 and 4 for a direct- and indirect-band-gap semiconductor, respectively [31]. The plot of $(\alpha h\nu)^2$ versus $h\nu$ is shown in Fig. 5b, and the E_g values are calculated by estimating the intercept of the tangent to the plot. So in this study, the band gaps of TiO₂ and AgInS₂ are estimated to be about 3.30 and 1.75 eV, respectively, whereas the band gap of heterostructure AT-5 to be about 2.75 eV. In addition, the band gaps of AT-1, AT-3 and AT-10 are calculated to 1.75, 2.0 and 2.98 eV (shown in Fig. S1 in the SI).

3.3.2. SPV spectra

SPV spectroscopy, as a well-established non-contact method, could indicate effective spatial separation properties of photoinduced charges under monochromatic excitation. Generally, a stronger SPV response signal implies a higher separation efficiency of photo-generated charges under the illuminated condition [32]. The ac SPV amplitude spectra of all the samples are shown in Fig. 6. It is obvious that the signals of AT-5 and AT-10 exhibit higher response than that of TiO₂, AgInS₂ and other composites in the visible-light region ($\lambda > 400$ nm), indicating that the

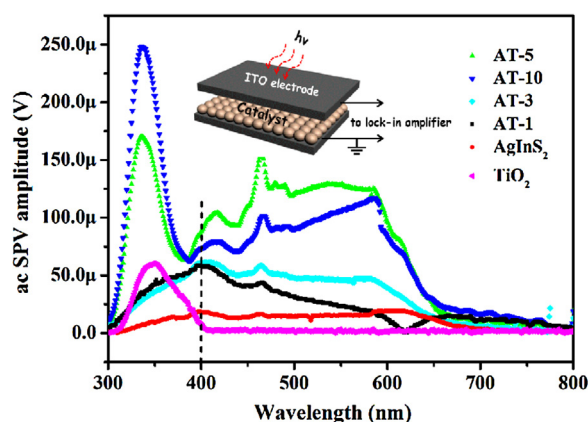


Fig. 6. SPV amplitude spectra for the samples. Inset: schematic of ac SPV measurement configurations for the samples.

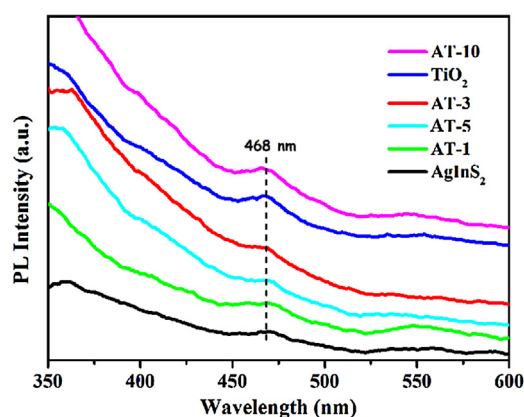


Fig. 7. PL spectra of the samples.

composite would enhance visible-light absorption and possess effective separation of photo-generated charges. The results are consistent with the analysis of the DRS characterization. Importantly, the SPV signals of all the composites are stronger than pristine materials (TiO₂ and AgInS₂), suggesting that the forming heterostructures with AgInS₂ would be beneficial for charges separation quickly.

3.3.3. PL spectra

As the catalytic materials are illuminated and then would release electrons from valence band, these hot photo-generated electrons with such high energy would easily relax to low energy level, which results in the occurrence of energy forms of heat or luminescence emission. So the PL spectrum is closely related to the recombination of excited electrons and holes [33]. As shown in Fig. 7, the spectra were recorded with the excitation wavelength at 325 nm at room temperature. According to the previous report [30,34], the typical emission peaks at 468 nm are attributed to the surface states related to recombination of the electron-hole pairs in TiO₂ and other composites with TiO₂. So the composites AT-1, AT-3 and AT-5 show weak fluorescence signals, indicating that the recombination of photo-generated carriers is inhibited greatly and furthermore the photoinduced electrons and holes would transfer to the surface of catalysts more effectively. However, TiO₂ and AT-10 exhibit strong fluorescence signals at this peak for a large amount of TiO₂, indicating that more recombination of photo-induced charges. Based on these optical properties of the catalysts, it is concluded that the synthetic AT-5 heterostructures show stronger absorption in the visible-light region.

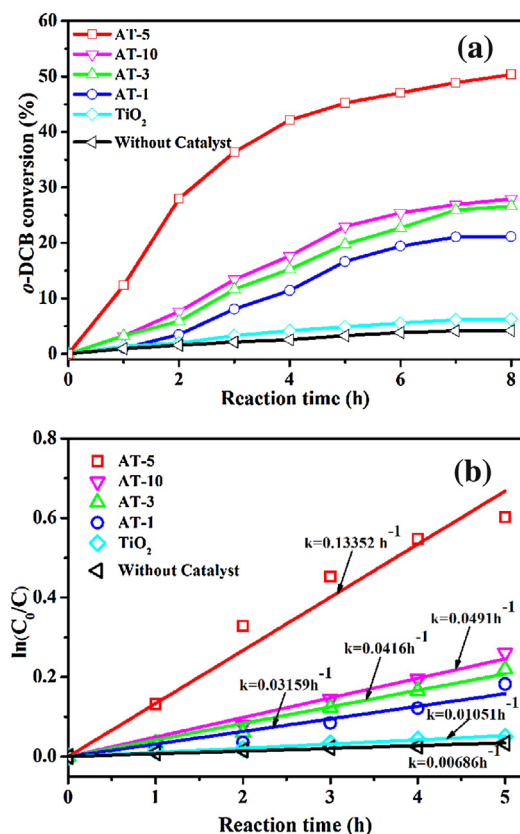


Fig. 8. (a) Photocatalytic degradation and (b) the kinetic curves of gaseous o-DCB over the obtained materials, respectively.

Importantly, the AT-5 material possesses lower recombination rate of photo-generated charge carriers in this region, indicating that it would be beneficial for enhancing the photocatalytic efficiency.

3.4. Activity and mechanisms analysis

3.4.1. Photocatalytic activity test

The photocatalytic degradation of gaseous o-DCB was investigated over these fabricated catalysts under visible light irradiation ($\lambda > 400$ nm). From Fig. 8a, o-DCB as a persistent organochlorine pollutant could hardly be decomposed without any catalysts under visible light. In regards to the TiO₂ (P25, Degussa), the pollutant conversion was just about 6.3% after 8 h reaction time, as P25 is UV responsive-only material. While the composites with AgInS₂ showed higher degradation ratios and the removal efficiency with the AT-5 could reach 50.4% after 8 h, which is attributed to the following reasons: (1) AgInS₂ material could be responsive to visible light; (2) The heterojunctions would promote separation and migration for photon-generated carriers. Compared with the AgInS₂ and other composites (AT-1, AT-3 and AT-10), AT-5 shows the highest photocatalytic activity and the probable reasons are as follows: (1) Based on SPV amplitude spectra for all the samples in Fig. 6, AT-5 catalyst shows the most intense SPV signal in the visible-light region ($\lambda > 400$ nm), indicating that AT-5 would possess the most effective spatial separation of photo-generated charges, which would be the determining factor for such higher efficiency. (2) Based on PL spectra for all the samples in Fig. 7, AT-5 catalyst shows weak fluorescence signals at 468 nm, indicating that the recombination of photo-generated carriers is inhibited greatly and furthermore the photoinduced electrons and holes would transfer to the surface of catalysts more effectively. In addition, the 5 h reaction time was selected to explore reaction kinetics as

Table 1

Crystal lattice parameters of orthorhombic AgInS₂.

| Parameters | a (Å) | b (Å) | c (Å) | $\alpha = \beta = \gamma / ^\circ$ |
|------------|-------|-------|-------|------------------------------------|
| Exp. | 7.001 | 8.278 | 6.698 | 90.0 |
| Calc. | 7.336 | 8.439 | 6.922 | 90.0 |

some intermediates generated were adsorbed on the surface of catalysts. According to an early report [35], the Langmuir–Hinshelwood model was chosen to fit the photocatalytic reaction by using a reaction rate equation: $\ln(C_0/C_t) = kt$, where C_0 is the initial concentration of gaseous o-DCB, C_t is the final concentration after t h degradation, k is the corresponding first-order kinetic constant, and t is reaction time. From Fig. 8b, it could be seen that all of the reactions follow pseudo-first-order curves, and the kinetic constant over AT-5 (0.13352 h^{-1}) is 12.7 times as great as TiO₂ (0.01051 h^{-1}), indicating that after coupling with AgInS₂, the degradation efficiency of gaseous o-DCB over these fabricated catalytic materials shows significant enhancement.

3.4.2. In situ FTIR study of degradation process of o-DCB

The *in situ* FTIR technique would be helpful to explore the reaction mechanisms on the surface of catalysts [28]. In this work, infrared transmission spectra (Fig. 9) of gaseous o-DCB degradation over the AT-5 were recorded under visible light irradiation. As shown in Fig. 9a, after adsorption equilibrium ($t = 0$), the strong absorption bands at 1435, 1458 and 1574 cm^{-1} could be ascribed to stretching vibrations of aromatic rings. Due to the formation of a π -complex between the unsaturated metal ions and aromatic ring on the crystal face of AT-5, these bands were shifted slightly [26], indicating that the adsorption mode of the o-DCB molecule plane is parallel to the crystal face of AT-5. In addition, the strong bands at 1128 and 1036 cm^{-1} (Fig. 9b) are attributed to the C–Cl symmetric and asymmetric stretching vibrations, respectively. As irradiation time passed, the bands discussed began to exhibit downtrend gradually. After 8 h reaction time, the degradation ratio was about 50%. Whereas, the bands at 2361 and 2339 cm^{-1} (Fig. 9c) corresponding to the stretching vibrations of C–O bonds from CO₂ increased, which could suggest that a quantity of gaseous o-DCB could be mineralized to CO₂.

3.5. Mechanism of enhanced photocatalytic activity

3.5.1. Structure optimization of AgInS₂

In order to explore the enhanced mechanism of AgInS₂/TiO₂ hetero-junction nanostructures for photocatalytic activity, crystalline and electronic structures of AgInS₂ should be investigated by first-principles calculation based on DFT. From XRD patterns of AgInS₂, the material is attributed to orthorhombic phase with space group PNA21 (NO. 33). As shown in Fig. 10, the structure contains eight sulfur atoms, four indium atoms and four silver atoms, and both Ag and In atoms have 4-fold coordination surrounded by four S atoms, while the S atoms have 4-fold coordination surrounded by two Ag atoms and two In atoms. Then the optimized parameters are $a = 7.336 \text{ Å}$, $b = 8.439 \text{ Å}$, $c = 6.992 \text{ Å}$, and all angles are 90° (Table 1). The calculated parameters of lattice constants are in very good agreement with experimental values within deviations of 2%. Regarding the chemical bonding properties in AgInS₂, the bond populations and atomic Müliken charges were investigated quantitatively. As calculated in Table 2, the bond populations between In and S atoms are from 0.41–0.50e, showing the covalent property. In addition, the populations of Ag–S bonds are from 0.27–0.35e, suggesting that the covalency between In and S atoms is greater than that between Ag and S atoms, which could affect the band edge positions of AgInS₂ [21].

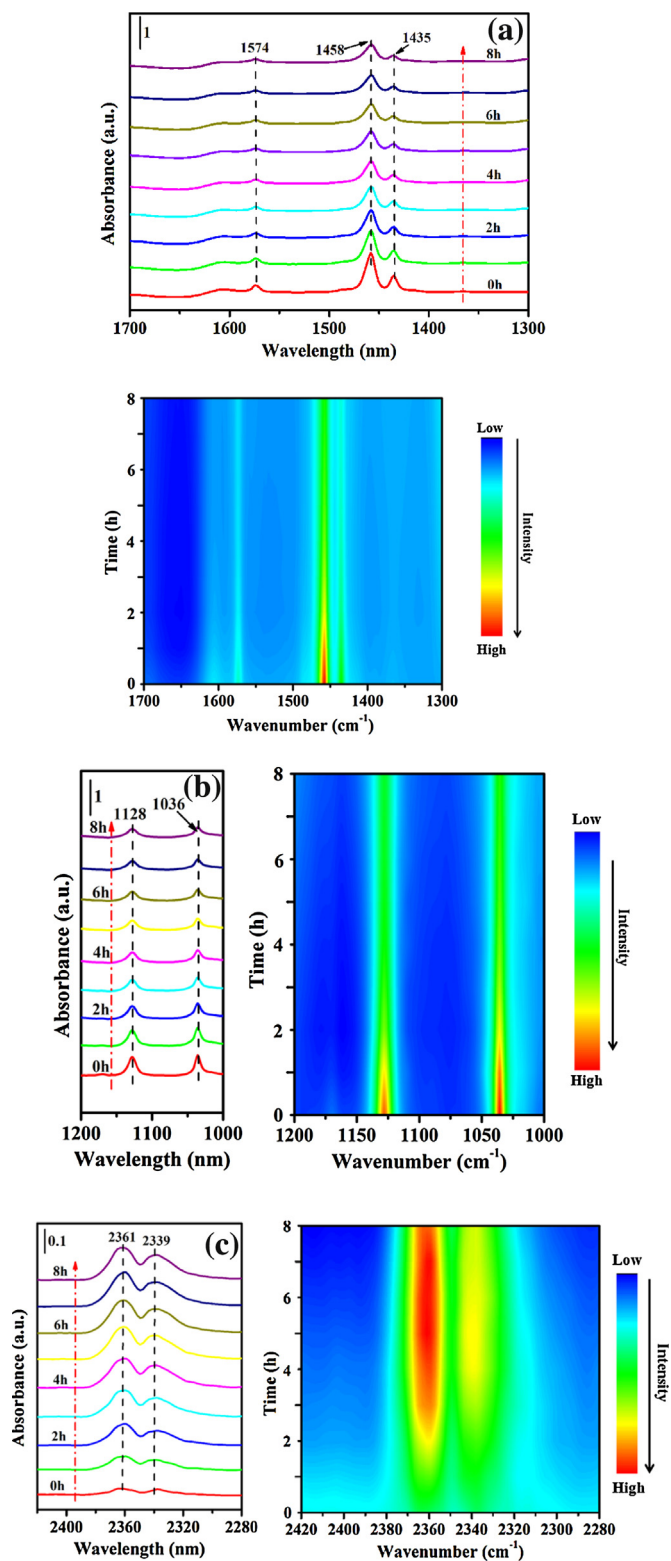


Fig. 9. (a–c) The FTIR spectra of degradation process for gaseous *o*-DCB over the AT-5 in the different regions and the corresponding time-domain IR spectra.

Moreover, it is obvious that the lengths of Ag–S and In–S bonds are unequal in the AgInS_2 crystal structure, which could give rise to the distortion in AgS_4 and InS_4 tetrahedra. According to the previous report [23], the distortion of tetrahedra could be significantly beneficial for separation of the centers of the positive charges and negative charges, and furthermore could form the dipole moments,

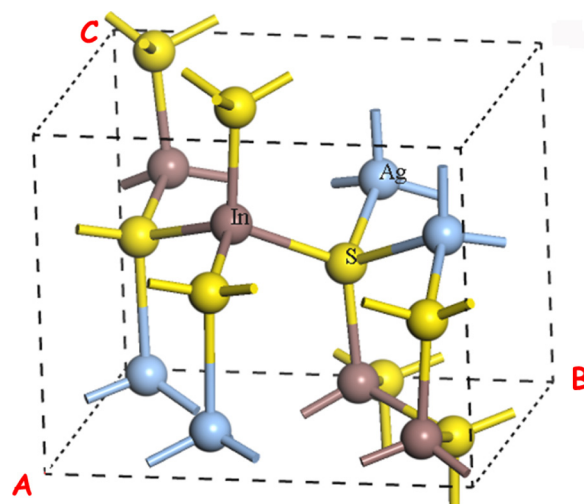


Fig. 10. Unit-cell structure of orthorhombic AgInS_2 . Yellow, brown, and blue spheres represent S, In, and Ag atoms, respectively. (For interpretation of the references to color in this figure legend, the reader is referred to the web version of this article.)

Table 2

The calculated parameters of bonds and charge in optimized AgInS_2 .

| Parameters | In...S | | | | Ag...S | | | |
|-------------------|---------|-------|-------|-------|---------|-------|-------|-------|
| Bond length (Å) | | | | | | | | |
| Calc. | 2.544 | 2.555 | 2.557 | 2.561 | 2.594 | 2.601 | 2.63 | 2.698 |
| Bond population | | | | | | | | |
| Calc. | 0.5 | 0.47 | 0.5 | 0.41 | 0.35 | 0.31 | 0.27 | 0.32 |
| Atomic Mulliken | | | | | | | | |
| Charge (e) | In 0.86 | | | | Ag 0.17 | | | |
| Calc. | −0.52 | −0.51 | −0.51 | −0.52 | −0.52 | −0.52 | −0.51 | −0.51 |
| Dipole moment (D) | | | | | | | | |
| Calc. | 0.16 | | | | 0.04 | | | |

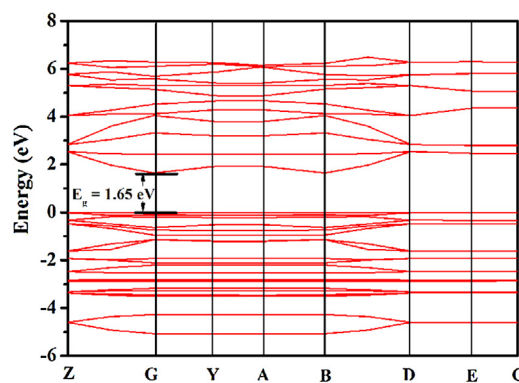


Fig. 11. Band structure of AgInS_2 . The 0 eV position is set to Fermi level.

which lead to the internal electric field. It has been reported that the internal electric field can promote the separation of photo-generated carriers and then enhance photocatalytic efficiency [23]. With the Mulliken charges and bond lengths (Table 2), the values of the dipole moments for AgS_4 and InS_4 tetrahedra are about 0.16 D and 0.04 D, respectively, indicating that the orthorhombic AgInS_2 material would be in favor of enhancement of photocatalytic activity.

3.5.2. Electronic structures of AgInS_2 and TiO_2

The electronic band structures and density of states (DOS) of optimized AgInS_2 crystal were calculated based on DFT method. As depicted in Fig. 11, the photocatalyst is a direct band-gap

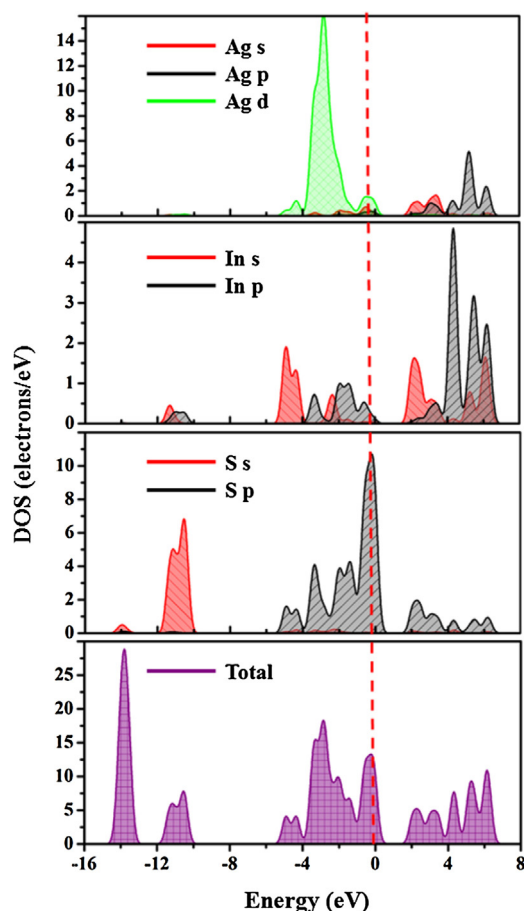


Fig. 12. TDOS and PDOS of orthorhombic AgInS₂. (For interpretation of the references to color in this figure legend, the reader is referred to the web version of this article.)

semiconductor and both the conduction bands minimum (CBM) and the valence bands maximum (VBM) are located at G point. Additionally, the calculated band-gap energy is around 1.65 eV, which is nearly consistent with the experimental value (about 1.75 eV), shown in Fig. 5b. Fig. 12 shows the calculated total density of states (TDOS) of orthorhombic AgInS₂, together with the partial DOS of silver, indium and sulphur elements. Nearby the Fermi level (a red dotted line), it is obvious that the top of the valence band (−2 to 0 eV) is mainly an antibonding state of Ag 4d and S 3p orbitals. Furthermore, the bottom of conduction band is also mainly attributed to the antibonding component of In 5s, S 3s and S 3p. In other words, the CBM is determined by the In–S interaction, while the VBM is dominated by the Ag–S interaction.

Likely, the structure optimization and DOS of optimized TiO₂ crystal were also calculated. From Fig. S2 in the SI, it could be seen that the bottom of the CB is dominated by the 2p orbital of the O element, and the top of the VB is occupied by the Ti 3d orbital. Therefore, when AgInS₂/TiO₂ composites are illuminated by visible light, the transition of electrons is inclined to occur from the Ag 4d and S 3p orbitals to the In 5s orbital of AgInS₂, and then to the O 2p orbital of TiO₂.

3.5.3. The band alignment analysis of TiO₂ and AgInS₂

The possible mechanism of photocatalytic degradation for gaseous *o*-DCB over the AgInS₂/TiO₂ hetero-junction nanostructures under visible-light irradiation can be proposed based on the energy level and electronic migration in Fig. 13. The conduction band (CB), valence band (VB) and Fermi level positions of AgInS₂ and TiO₂ are shown in Fig. 13a. For semiconductor AgInS₂, the CB

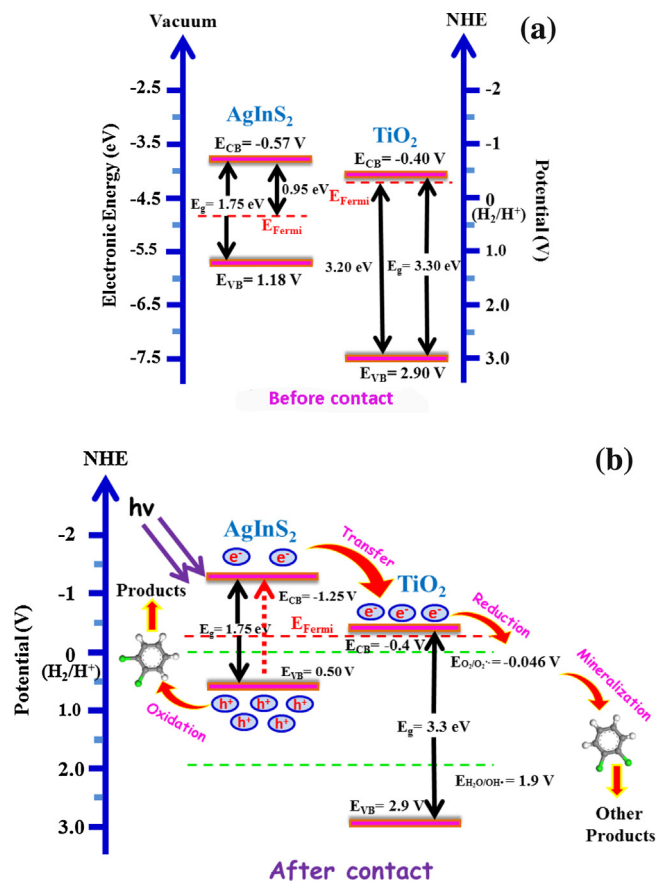


Fig. 13. A schematic of band-gap match and electron-hole pairs separation of the composite, (a) before contact, (b) after contact.

position is located at −0.57 V and the valence band 1.18 V, and the Fermi level is at 0.38 V [21,36]. Whereas, for *n*-type semiconductor TiO₂, the Fermi level is generally close to the CB potential (below 0.1–0.2 V), so the Fermi level in TiO₂ is located at around −0.3 V. When the heterojunction structure was formed by interaction with AgInS₂ and TiO₂, the Fermi level of composites could reach a balanced state due to the system equilibrium [37]. Consequently, the Fermi level position of AgInS₂ in the composites moved to −0.3 V, which was approximately equal to that of TiO₂ for the low content, and the balanced CB and VB are shown in Fig. 13b.

When the composites are irradiated by visible light, the electrons of AgInS₂ would be excited from VB to CB as it possesses a narrow band gap ($E_g = 1.75$ eV), and then the photo-generated electrons quickly transfer to the CB of TiO₂ due to more positive potential of *ca.* −0.4 V. In addition, the photogenerated holes (h^+) remain in the VB of AgInS₂, and could directly react with gaseous *o*-DCB to form some products with strong oxidation ability. According to the potential of H₂O/OH•, the holes (h^+) would not oxidize the absorbed H₂O to hydroxyl radicals (OH•) for more positive potential ($E = 1.9$ V) [38]. However, excited electrons (e^-) can be reduced to O₂•− with O₂ adsorbed on the surface of catalyst due to a more positive potential ($E = -0.046$ V), which was verified by electron paramagnetic resonance (EPR) technique. As depicted in Fig. 14, the characteristic signals of the DMPO-O₂•− were captured under visible-light irradiation, indicating that O₂•− was generated. However, there are no distinct EPR peaks in the dark for lacking of the active species, so the light radiation is a crucial step. Lastly, the superoxide radicals could mineralize adsorbed *o*-DCB to form other products.

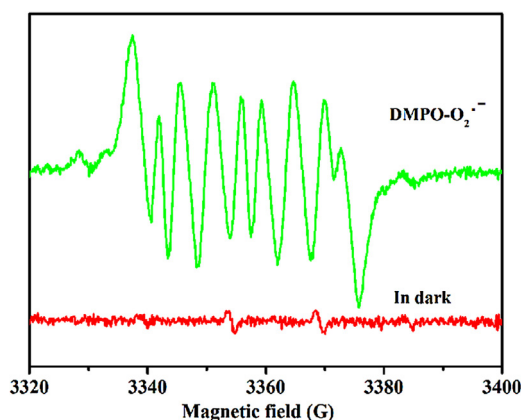


Fig. 14. EPR spectra in AT-5 methanol suspension solution after 40 s under visible light irradiation ($\lambda > 400$ nm).

4. Conclusions

In conclusion, the TiO_2 and AgInS_2 heterostructures with different molar ratios were fabricated through a simple one-pot hydrothermal method. The synthesized photocatalysts exhibited higher conversions for photocatalytic degradation of gaseous *o*-DCB under visible light. Notably, the degradation rate of AT-5 could reach about 50%. More importantly, the mechanism for enhanced photocatalytic activity is elucidated based on optical properties, DFT and band alignment. Such novel catalysts could meet the demands for CI-VOCs purification in the ambient environment.

Acknowledgments

This work was supported financially by the National Nature Science Foundation of China (No. 21377015) and the Key Laboratory of Industrial Ecology and Environmental Engineering, China Ministry of Education.

Appendix A. Supplementary data

Supplementary data associated with this article can be found, in the online version, at <http://dx.doi.org/10.1016/j.apcatb.2015.12.003>.

References

- [1] S. Yurdakal, G. Palmisano, V. Loddo, V. Augugliaro, L. Palmisano, *J. Am. Chem. Soc.* 130 (2008) 1568–1569.
- [2] Q. Wang, M. Zhang, C.C. Chen, W.H. Ma, J.C. Zhao, *Angew. Chem. Int. Ed.* 49 (2010) 7976–7979.
- [3] X.B. Chen, L. Liu, P.Y. Yu, S.S. Mao, *Science* 331 (2011) 746–750.

- [4] A. Abdal-hay, A.S.H. Makhlof, K.A. Khalil, *ACS Appl. Mater. Interfaces* 7 (2015) 13329–13341.
- [5] K. Li, B. Chai, T.Y. Peng, J. Mao, L. Zan, *ACS Catal.* 3 (2013) 170–177.
- [6] M. Es-Souni, M. Es-Souni, S. Habouti, N. Pfeiffer, A. Lahmar, M. Dietze, C.H. Solterbeck, *Adv. Funct. Mater.* 20 (2010) 377–385.
- [7] S. Linic, P. Christopher, D.B. Ingram, *Nat. Mater.* 10 (2011) 911–921.
- [8] Z.H. Zhang, L.B. Zhang, M.N. Hedhili, H.N. Zhang, P. Wang, *Nano Lett.* 13 (2013) 14–20.
- [9] H.U. Lee, S.C. Lee, S.H. Choi, B. Son, S.J. Lee, H.J. Kim, J. Lee, *Appl. Catal. B: Environ.* 129 (2013) 106–113.
- [10] W.W. Fu, S. Ding, Y. Wang, L.L. Wu, D.M. Zhang, Z.W. Pan, R.W. Wang, Z.T. Zhang, S.L. Qiu, *Dalton Trans.* 43 (2014) 16160–16163.
- [11] J. Wang, C.Y. Fan, Z.M. Ren, X.X. Fu, G.D. Qian, Z.Y. Wan, *Dalton Trans.* 43 (2014) 13783–13791.
- [12] S.A. Moniz, S.A. Shevlin, X.Q. An, Z.X. Guo, J.W. Tang, *Chem. Eur. J.* 20 (2014) 15571–15579.
- [13] H.T. Ren, S.Y. Jia, J.J. Zou, S.H. Wu, X. Han, *Appl. Catal. B: Environ.* 176–177 (2015) 53–61.
- [14] H.F. Li, H.T. Yu, X. Quan, S. Chen, H.M. Zhao, *Adv. Funct. Mater.* 25 (2015) 3074–3080.
- [15] T. Pons, E. Pic, N. Lequeux, E. Cassette, L. Bezdetnaya, F. Guillemin, F. Marchal, B. Dubertret, *ACS Nano* 4 (2010) 2531–2538.
- [16] W.S. Song, H. Yang, *Chem. Mater.* 24 (2012) 1961–1967.
- [17] K. Zhang, L.J. Guo, *Catal. Sci. Technol.* 3 (2013) 1672–1690.
- [18] R.G. Xie, M. Rutherford, X.G. Peng, *J. Am. Chem. Soc.* 131 (2009) 5691–5697.
- [19] B.D. Mao, C.H. Chuang, J.W. Wang, C. Burda, *J. Phys. Chem. C* 115 (2011) 8945–8954.
- [20] S.P. Hong, H.K. Park, J.H. Oh, H. Yang, Y.R. Do, *J. Mater. Chem.* 22 (2012) 18939–18949.
- [21] J.J. Liu, S.F. Chen, Q.Z. Liu, Y.F. Zhu, Y.F. Lu, *Comp. Mater. Sci.* 91 (2014) 159–164.
- [22] Z.P. Liu, K.B. Tang, D.K. Wang, L.L. Wang, Q.Y. Hao, *Nanoscale* 5 (2013) 1570–1575.
- [23] J. Sato, H. Kobayashi, Y. Inoue, *J. Phys. Chem. B* 107 (2003) 7970–7975.
- [24] Q. Liu, H. Lu, Z.W. Shi, F.L. Wu, J. Guo, K.M. Deng, L. Li, *ACS Appl. Mater. Interfaces* 6 (2014) 17200–17207.
- [25] T.T. Li, X.Y. Li, Q.D. Zhao, Y. Shi, W. Teng, *Appl. Catal. B: Environ.* 156–157 (2014) 362–370.
- [26] B.H. Aristizabal, C.M. Correa, A.I. Serykh, C.E. Hetrick, M.D. Amiridis, *J. Catal.* 258 (2008) 95–102.
- [27] A. Sobek, H.P.H. Arp, K. Wiberg, J. Hedman, G. Cornelissen, *Environ. Sci. Technol.* 47 (2013) 781–789.
- [28] B.J. Liu, X.Y. Li, Q.D. Zhao, J. Ke, J. Liu, S.M. Liu, M. Tadé, *J. Colloid Interfaces Sci.* 438 (2015) 1–6.
- [29] M. Segall, P.J.D. Lindan, M. Probert, C. Pickard, P. Hasnip, S. Clark, M. Payne, *J. Phys. Condens. Matter* 14 (2002) 2717.
- [30] J.J. Sun, X.Y. Li, Q.D. Zhao, J. Ke, D.K. Zhang, *J. Phys. Chem. C* 118 (2014) 10113–10121.
- [31] S. Li, Y.H. Lin, B.P. Zhang, Y. Wang, C.W. Nan, *J. Phys. Chem. C* 114 (2010) 2903–2908.
- [32] A.S. Zhu, Q.D. Zhao, X.Y. Li, Y. Shi, *ACS Appl. Mater. Interfaces* 6 (2014) 671–679.
- [33] Q.C. Xu, D.V. Wellia, Y.H. Ng, R. Amal, T.T.Y. Tan, *J. Phys. Chem. C* 115 (2011) 7419–7428.
- [34] Y. Lei, L.D. Zhang, G.W. Meng, G.H. Li, X.Y. Zhang, C.H. Liang, W. Chen, S.X. Wang, *Appl. Phys. Lett.* 78 (2001) 1125–1127.
- [35] J.H. Xu, W.Z. Wang, M. Shang, S.M. Sun, J. Ren, L. Zhang, *Appl. Catal. B: Environ.* 93 (2010) 227–232.
- [36] R. Bose, G. Manna, S. Jana, N. Pradhan, *Chem. Commun.* 50 (2014) 3074–3077.
- [37] Y. Hu, D.Z. Li, Y. Zheng, W. Chen, Y.H. He, Y. Shao, X.Z. Fu, G.C. Xiao, *Appl. Catal. B: Environ.* 104 (2011) 30–36.
- [38] J. Schneider, M. Matsuoka, M. Takeuchi, J.L. Zhang, Y. Horiuchi, M. Anpo, D.W. Bahnemann, *Chem. Rev.* 114 (2014) 9919–9986.